Discrimination experiments with the U.S. Army's standard metal detector

Lloyd Riggs,[1] Sailaja Chilaka,[1] Leslie Collins,[2] Larry Lowe,[3] and Richard Weaver[4]

Received 2 August 2003; revised 13 January 2004; accepted 28 January 2004; published 1 July 2004.

[1] Discrimination experiments with the U.S. Army's standard hand-held metal detector (AN/PSS-12) are described. An appendix describes the functioning of the device as a metal detector, and the body of the paper discusses modifications to the device necessary to carry out the discrimination experiments. Half of the mines in a large blind test grid were correctly identified with nearly zero false alarms, but the false alarm rate increased substantially for detection probabilities greater than one half. Degradation in performance is attributed to low signal-to-noise ratio from low metallic content mines buried deep in the soil. One measurement was taken with the object centered with respect to the search coils and four more with the object between the concentric search coils in the north, south, east, and west directions. Discrimination performance using all spatial measurements was shown to be superior to that obtained when using only the centered measurement, indicating that spatial measurement diversity is needed to adequately define all the unique modes of a target's polarizability tensor. *INDEX TERMS:* 0694 Electromagnetics: Instrumentation and techniques; 6909 Radio Science: Electromagnetic metrology; 6969 Radio Science: Remote sensing; *KEYWORDS:* discrimination, electromagnetic induction, metal detectors

Citation: Riggs, L., S. Chilaka, L. Collins, L. Lowe, and R. Weaver (2004), Discrimination experiments with the U.S. Army's standard metal detector, *Radio Sci.*, *39*, RS4S06, doi:10.1029/2003RS002955.

1. Introduction

[2] The magnitude of the worldwide mine problem is indeed serious, with the U.S. State Department estimating that a total of 45–50 million mines remain to be cleared [*MacDonald et al.*, 2003]. Additionally, it has been estimated that land mines claim an estimated 15,000–20,000 victims per year in 90 countries [*MacDonald et al.*, 2003]. Many different sensing technologies have been brought to bear on the mine problem, including: electromagnetic induction (EMI), ground-penetrating radar (GPR), X-ray backscatter, infrared/hyperspectral, acoustic/seismic, biological (dogs, bees, bacteria), etc. Except for the dog and common metal detector (MD) (an EMI device), most of these sensing methods are to this day somewhat immature, but research continues toward improving their viability [*MacDonald et al.*, 2003]. A noteworthy exception is the Handheld Standoff Mine Detection System (HSTAMIDS), a U.S. Army system currently completing development. HSTAMIDS, now referred to as the AN/PSS-14, is a dual-technology sensor combining GPR and MD.

[3] The common metal detector is probably the most ubiquitous EMI device in use today. A recent report by *Das et al.* [2000] compares the sensitivity and operating characteristics of metal detectors manufactured by no fewer than twelve different companies, many of which offer several models. Treasure hunters and hobbyists probably constitute the largest commercial market for these devices, but many units are also used by armed forces worldwide for humanitarian demining as well as for mine field breaching operations.

[4] Modern metal detectors can achieve the necessary sensitivity to detect buried low metallic (LM) content land mines (so-called plastic land mines) that contain only a few grams of metal [*Riggs*, 1999]. Examples of modern-day metal detectors include the U.S. Army's standard issue AN/PSS-12 manufactured by Schiebel Corporation of Austria and the F3 manufactured by Minelab Corporation of Australia. Unfortunately, as the name implies, a metal detector will produce an audio alarm whenever any metallic object is brought near its

[1]Electrical and Computer Engineering Department, Auburn University, Auburn, Alabama, USA.
[2]Electrical and Computer Engineering Department, Duke University, Durham, North Carolina, USA.
[3]Phase IV Systems, Huntsville, Alabama, USA.
[4]Night Vision and Electronic Sensors Directorate, Fort Belvoir, Virginia, USA.

0048-6604/04/2003RS002955

search coil(s). At present, commercially available metal detectors have very limited ability to discriminate between land mines and buried metallic clutter. For example, Minelab, whose EMI instrumentation is frequently used in humanitarian demining operations, reports that it is not uncommon to remove 1000 metallic clutter items per mine (http://www.countermine.minelab.com). In short, metallic clutter can be considered the nemesis of the metal detector.

[5] This paper addresses detection and discrimination experiments carried out with the U.S. Army's standard handheld metal detector the AN/PSS-12 (http://www.schiebel.net/pages/prod_an19.html). Our primary interest is to investigate methods of reducing false alarms, or in the parlance of detection theory, we are interested in the binary hypothesis problem, mine or no mine, and we seek to maximize probability of detection, P_D, while simultaneously minimizing probability of false alarm, P_{FA}. We have less interest in the detection problem except for the obvious constraint that without sufficient signal-to-noise ratio, discrimination is impossible. However, as stated above, the best modern-day metal detectors are quite sensitive, able to detect mostly plastic antipersonnel (AP) and antivehicular (AT) mines buried as deep as 6 inches.

[6] The organization of the paper is as follows: first, a theory of continuous wave and pulsed electromagnetic induction devices is presented with treatment of the problem given in both frequency and time domains. Next, modifications to the AN/PSS-12 necessary to carry out the discrimination experiments are described. An appendix is included that describes the operation of AN/PSS-12 as a metal detector. Next, an overview of the JUXOCO test site is given, including a description of the calibration and blind grids and the type of mines and clutter objects buried therein. Also, this section describes the method of data collection, including the orientation of the search coils with respect to the target for each measurement as well as the postprocessing procedures used to acquire the target's EMI response function. Details of the discrimination algorithm and its performance are given in the last part of the paper, followed by conclusions and suggestions for other areas of fruitful research.

2. Theory of Electromagnetic Induction Devices

[7] A thorough introduction to the theory of electromagnetic induction can be found in the work of *Grant and West* [1965, chap. 17] or in a somewhat more recent work by *Baum* [1999, chap. 6]. The topic shall be addressed briefly here but only as it pertains to the operational characteristics of metal detectors and to the issue of discriminating between metallic clutter and mines.

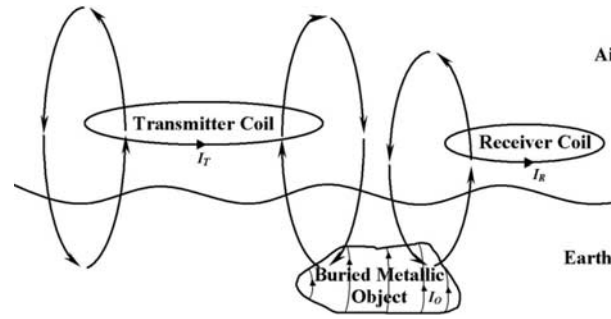

Figure 1. Typical electromagnetic induction system.

[8] First, consider the general electromagnetic induction system of Figure 1, composed of a transmitter coil, receiver coil, and buried metallic object. Electric currents that flow in the transmitter coil radiate a primary magnetic field that penetrates the surrounding medium and any nearby metallic object. In accordance with Faraday's law, this primary field will cause eddy currents to flow on and within the buried object. The object eddy currents radiate a scattered magnetic field that will in turn induce a voltage into the receiver coil, again in accordance with Faraday's law. In general, there will also be direct coupling between the transmitter and receiver (although techniques exist for minimizing this), so that the net voltage at the receiver will be the superposition of the direct and object coupled parts. The receiver voltage is used to detect the target or, more importantly here, to distinguish one target from another.

[9] Induced eddy currents depend on the object's constitutive parameters (conductivity σ and permeability μ) and geometry as well as coupling strength between the transmitter coil and object. At low frequencies (typically less than 100 kHz), displacement currents may be neglected, and if Earth is assumed nonmagnetic ($\mu_{\text{Earth}} = \mu_o$), with conductivity much less than that of the object ($\sigma_{\text{Earth}} \ll \sigma$), then the coils and object might as well be immersed in vacuum.

[10] The assumption that the response of a metal detector is independent of Earth's constitutive parameters is certainly convenient for purposes of exposition but is not necessarily realistic. There are many regions in the world that have highly conductive and/or magnetic soils and a well-designed metal detector must have some means of eliminating (or reducing to an acceptable level) the ground response without sacrificing overall detector sensitivity. A paper by *Corbyn* [1980] and a U.S. patent by *Candy* [1996] discuss methods of eliminating this undesirable effect of soil. The metal detector component of the HSTAMIDS unit mentioned in the introduction is

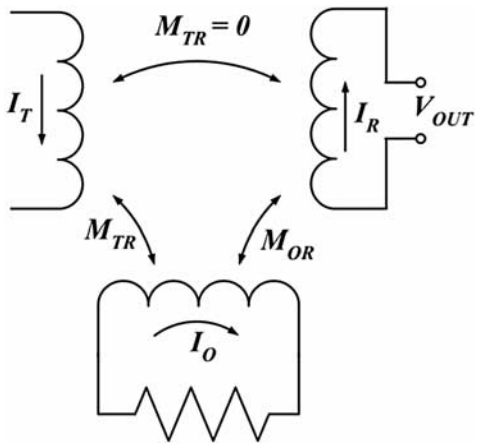

Figure 2. Equivalent circuit of an EMI system.

manufactured by Minelab Inc., and its design principles are also described by *Candy* [1996].

[11] Figure 2 presents a simple equivalent circuit of the EMI system of Figure 1. The buried object is represented by an inductance L_O in series with resistance R_O. Mutual coupling between the transmitter coil and object, M_{TO}, gives rise to object current I_O. Likewise, mutual coupling between the buried object and open-circuited receiver coil, M_{OR}, gives rise to that component of the total receiver voltage due to the buried object, V_{OBJECT}. Finally, mutual coupling between transmitter and receiver coils, M_{TR}, gives rise to V_{DIRECT}, and by superposition, $V_{\mathrm{OUT}} = V_{\mathrm{OBJECT}} + V_{\mathrm{DIRECT}}$. In terms of the circuit parameters of Figure 2,

$$V_{\mathrm{DIRECT}} = j\omega M_{TR} I_T, \tag{1}$$

and

$$V_{\mathrm{OBJECT}} = j\omega M_{OR} I_O. \tag{2}$$

Kirchhoff's voltage law applied to the object loop yields

$$I_O(R_O + j\omega L_O) + j\omega M_{TO} I_T = 0. \tag{3}$$

Eliminating the object current and carrying out a few steps of algebra results in

$$\frac{V_{\mathrm{OBJECT}}}{V_{\mathrm{DIRECT}}} = \frac{-M_{TO}M_{OR}}{L_O M_{TR}} \frac{\alpha^2 + j\alpha}{1+\alpha^2}, \tag{4}$$

where $\alpha = \omega\tau$ and $\tau = L_O/R_O$ are the time constant of the object. Mutual coupling between circuits I and j may be defined in terms of a coupling coefficient as

$$M_{ij} = k_{ij}\sqrt{L_i L_j}, \tag{5}$$

with $|k_{ij}| \leq 1$. Using equation (5) in equation (4) gives the final desired form of the object transfer function

$$\frac{V_{\mathrm{OBJECT}}}{V_{\mathrm{DIRECT}}} = \frac{-k_{TO}k_{OR}}{k_{TR}} \frac{\alpha^2 + j\alpha}{1+\alpha^2}. \tag{6}$$

The response function (6) conveniently separates into the product of two terms, a coupling coefficient $k_{TO}k_{OR}/k_{TR}$, and frequency-dependent term $(\alpha^2 + j\alpha)/(1 + \alpha^2)$. The numerator of $k_{TO}k_{OR}/k_{TR}$ is coupling from the transmitter to receiver by way of the object, whereas k_{TR} is direct coupling between transmitter and receiver. Coupling depends on the orientation of the object with respect to the transmitter and receiver coils but not on frequency. Note that, in general, it is desirable to reduce direct coupling between transmitter and receiver as much as possible, thereby maximizing response magnitude, but k_{TR} can never be zero, as some finite (albeit small) direct coupling will always exist between transmitter and receiver coils. As shown in Figure 3, the real part of $(\alpha^2 + j\alpha)/(1 + \alpha^2)$ approaches unity at high frequencies (α approaches infinity), while the imaginary part approaches zero. At the crossover frequency $\alpha = 1$, or $f_{\mathrm{CROSSOVER}} = 1/(2\pi\tau) = R_0/(2\pi L_0)$, the real and imaginary parts are equal, the phase is 45°, and the magnitude is approximately 3 dB below its asymptotic value. Succinctly put, the object behaves as a single pole high pass filter.

[12] Before continuing, we point out that in the development of equation (6), the object was assumed to be a simple first-order target. An example of a simple first-order target is a loop of thin copper wire (radius of wire much less than radius of loop), sometimes referred to as a *q* coil. The cylinder and sphere are not simple first-order targets, and their crossover frequency, as defined above, is not coincident with the quadrature (imaginary part)

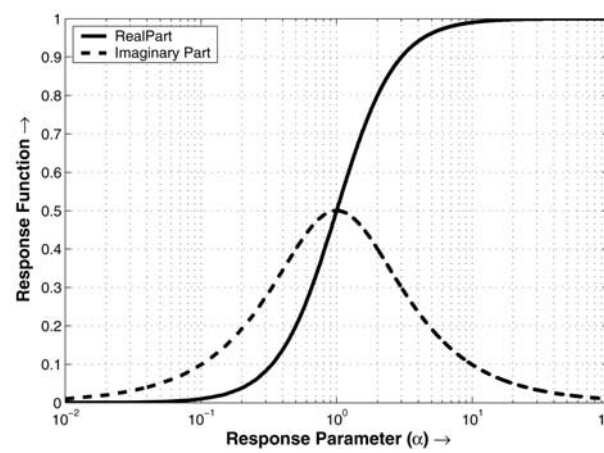

Figure 3. Normalized response of a simple first-order target.

peak. Also, magnetic targets (targets whose relative permeability is not unity, e.g., steel) exhibit a real part that is negative below some frequency [*Grant and West*, 1965].

[13] *Liao and Carin* [2004] give

$$M(\omega) = diag\left[m_{p0} + \sum_k \frac{\omega m_{pk}}{\omega - j\omega_{pk}}, m_{p0} + \sum_k \frac{\omega m_{pk}}{\omega - j\omega_{pk}}, m_{z0} + \sum_k \frac{\omega m_{zk}}{\omega - j\omega_{zk}}\right] \quad (7)$$

as the magnetization tensor of a rotationally symmetric object with the z direction taken as the axis of rotation. (The object's scattered field is proportional to its magnetization tensor.) Here we observe that each component of the magnetization tensor is composed of an infinite sum of high pass terms of weight m_{zk} and m_{pk} for the component along and perpendicular to the object's axis of rotation respectively. Unlike the simple object treated above, the frequency response of arbitrarily shaped conducting bodies is represented by a superposition of high pass terms, but in many cases, only the lowest-order component has significant strength allowing one to replace the summation in $M(\omega)$ with a single term as given in equation (6) [*Carin et al.*, 2001]. If the excitatory magnetic field is aligned with the axis of the object, then all m_{pk} are zero and visa versa, but in general, both components will be excited. Also, m_{p0} and m_{z0} give the DC (zero frequency) response and both are zero for nonmagnetic targets.

[14] Metal detectors are usually designed to operate as either continuous wave (CW) or pulsed devices. In the former case the detector may operate at a single frequency, a few frequencies, or at many discrete frequencies over a bandwidth from say, some f_{low} to f_{high}, with f_{low} typically greater than 30 Hz and f_{high} less than 100 kHz [*Won et al.*, 1997]. Pulsed devices, as the term implies, use short pulses of current in the transmitter coil to excite eddy currents in the object, then the object radiated field is sensed by the receiver coil during the period of time between consecutive transmitter pulses. The AN/PSS-12 and F3 are both pulsed detectors, with the former utilizing distinct coils for transmit and receive, while the latter uses only a single coil. Clearly, the theory presented above is appropriate for CW detectors and indirectly applicable to pulsed detectors since time and frequency descriptions are Fourier transform pairs. However, it is usually instructive, and simpler, to describe pulsed operation by working directly in time domain.

[15] Generally speaking, at least for pulse induction systems, it is advantageous to force current through the transmitter coil and then extinguish it (turn it off) as rapidly as possible without oscillations. The reason for this can be attributed to the fact that the induced voltage in the object is proportional to the derivative of the transmitter current. Therefore a rapidly changing transmitter current will naturally induce a larger voltage in the object than will a slowly changing transmitter current; all other parameters held constant.

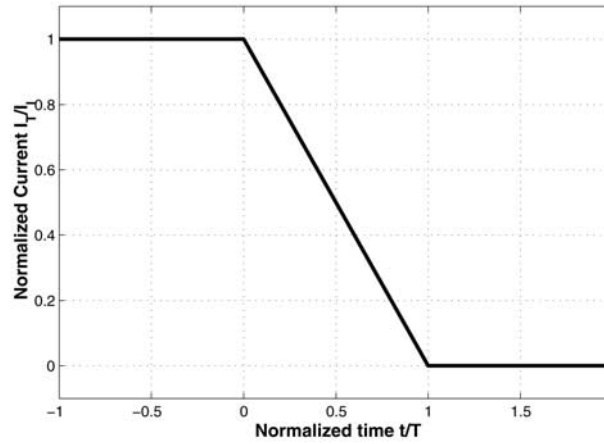

Figure 4. Plot of current I_T.

[16] Figure 4 defines a transmitter current I_T that linearly decreases from maximum to zero in a time T

$$I_T = I_I\left[u(t) - \frac{t}{T}u(t) + \left(\frac{t-T}{T}\right)u(t-T)\right], \quad (8)$$

where I_I is the value of I_T for all $t < 0$ (initial condition), $u(t)$ is the usual unit step function (zero for $t \leq 0$ unity for $t > 0$), and $u(t - T)$ is identical except that it "turns on" at T. Still referring to the simple equivalent circuit of Figure 2, the object and transmitter currents, $I_O(t)$ and $I_T(t)$, respectively, are related by

$$M_{TO}\frac{dI_T}{dt} = -R_O I_O(t) - L_O\frac{dI_O(t)}{dt}. \quad (9)$$

Substituting equation (8) into equation (9), invoking the Laplace transform, and carrying out a few steps of algebra yields

$$I_o(s) = -\frac{M_{TO}I_I}{T}\left[\frac{e^{-sT}-1}{s(R_O + sL_O)}\right], \quad (10)$$

which goes over into time domain as

$$I_O(t) = \frac{M_{TO}I_I\tau}{L_O T}\left\{\left(1 - e^{-t/\tau}\right)u(t) - \left(1 - e^{-(t-T)/\tau}\right)u(t-T)\right\}. \quad (11)$$

The final result is quite simple and consists of two terms, one that turns on at $t = 0$ and the other that turns on only

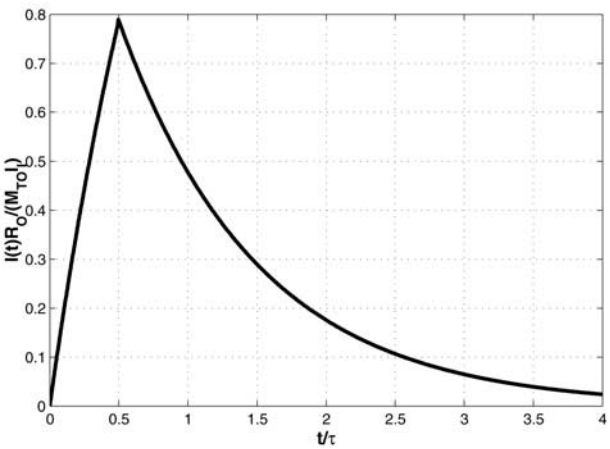

Figure 5. Normalized object current, $(I(t)R_O)/(M_{TO}I_I)$ versus normalized time t/τ, for a ratio of current-turn-off-time-to-object-time-constant of 0.5, $T/\tau = 0.5$.

after a time T. As shown in Figure 5, the object current increases exponentially with time constant $\tau = L_0/R_0$ to a maximum value given by $M_{TO}I_I\tau(1 - e^{-T/\tau})/L_oT$ and then decays exponentially, again with time constant $\tau = L_0/R_0$.

[17] Once again, the receiver coil output voltage has two components, one due to coupling between object and receiver and the other due to direct coupling between transmitter and receiver, or

$$V_R(t) = -M_{OR}\frac{dI_O(t)}{dt} - M_{TO}\frac{dI_T(t)}{dt}. \qquad (12)$$

Direct coupling between transmitter and receiver, second term in equation (12), just results in a voltage pulse of strength $M_{TO}I_I/T$ for $0 < t < T$ and zero otherwise. Coupling between the object and receiver coil gives rise to

$$V_{OC}(t) = \frac{-M_{TO}M_{OR}I_I}{TL_O}\left(\mathrm{e}^{-t/\tau}u(t) - e^{-(t-T)/\tau}u(t-T)\right). \qquad (13)$$

At $t = 0$ $V_{OC} = -M_{OR}M_{TO}I_I/L_OT$ and at $t = T$ $V_{OC} = M_{OR}M_{TO}I_I/L_O\tau$, where $(e^{-T/\tau} - 1)$ has been replaced with $-T/\tau$ accurate when $T/\tau \ll 1$, this must be the case if the system is to have sensitivity to an object with time constant τ. It is probably worth mentioning that the values of V_{OC} at $t = 0$ and $t = T$ agree with those of *Grant and West* [1965] except for a minus sign. The minus sign results from the fact that our current starts at I_I and linearly decays to zero, whereas the current in the work of *Grant and West* [1965] starts at zero and linearly increases to I_I (one slope is the negative of the other). The most important issue here is that after a time $t = T$ the object-induced receiver voltage just decays exponentially with time constant $\tau = L_0/R_0$.

[18] Just as above with our frequency domain expressions, the simple direct time domain solution provided here is correct only for first-order objects, and the response of a general object is described using a superposition of exponentially decaying terms each with a unique time constant and amplitude [*Baum*, 1999, chap. 6].

[19] One can think about discrimination either in terms of object decay rates (time domain) or real axis poles (frequency domain), whichever is more convenient. Very basically, discrimination among a set of objects is carried out by comparing their decay rates (or poles). The idea is to assemble a library of decay rates (or poles) for each expected target, and then some measure of "best fit" is used to select the object in the library whose response most closely matches the data. Measurements are always contaminated by noise, so the discrimination problem is really one of inference from incomplete information. More will be said regarding this issue in section 5.

3. Modifications to the AN/PSS-12 for Discrimination Experiments

[20] This section describes modifications to the AN/PSS-12 necessary to record an undistorted representation of an object's response function. Appendix A describes the function of the device as a metal detector without modifications to its circuitry.

[21] One can observe that the voltage waveform after the first stage of amplification following the receiver coil deviates significantly from the exponential response that would be expected on the basis of the theory presented in section 2. Since our discrimination approach requires high-fidelity undistorted target information, we decided to bypass all the AN/PSS-12's receiver circuitry and acquire data at the output of the receiver coil. Two cascaded AD-524A instrumentation amplifiers with a combined gain of 60 dB and upper 3 dB frequency of approximately 100 kHz were used to boost the weak receiver coil signal. Also, in order to avoid oscillations, it was necessary to place a resistor in parallel with the receiver coil so that the coil inductance, its parasitic capacitance, and the applied shunt resistor form a critically damped second-order system. A National Instruments Scope Card, NI-5102 with 15 MHz bandwidth, 20 MHz maximum sampling frequency, and an 8-bit analogue-to-digital converter, was used to sample the amplified receiver coil voltage. The NI-5102 card plugs into the PCMCIA slot of a laptop computer and is controlled with standard LabView software. Figure 6 shows the components of the data acquisition system.

Figure 6. Modified data acquisition system.

[22] The transmitter circuitry of the AN/PSS12 was also modified to produce a single linear ramp with superior spectral content compared to that of the symmetrical waveform of Figure 7. Notice that according to Figure 8, the spectral content of the unmodified (bipolar current) waveform has no DC component and, owing to odd symmetry, exhibits oscillations, whereas the modified (unipolar current) waveform has finite energy at zero frequency and is devoid of oscillations. It was also necessary to place a resistor in parallel with the receiver coil in order to avoid oscillatory behavior when the transmitter current is quenched.

[23] Laboratory tests were carried out to ensure that the modifications described above produced measured waveforms in agreement with theory. As described in greater detail elsewhere [*Lowe*, 2001], measurements were made of a large number of thin copper wire loops (q coils) and a 2.0 cm diameter chrome-steel sphere. The loop wire diameter (gauge) and circumference were adjusted to produce waveforms with a variety of decay rates. Decay rates extracted from the measured data using an iterative numerical method known as differential corrections were compared to theoretical values computed from the ratio of wire loop resistance to inductance [*Chapman and Kirk*, 1970]. In every case, measurement and theory were in good agreement. Low metallic content land mines were also measured, and since their extracted decay rates were bounded by those of the copper loops, we concluded that the system should, at least in principle, be effective for discrimination purposes. Figure 9 shows measurements compared to theoretical data for the 2.0 cm diameter chrome-steel sphere ($\mu_r = 28$, $\sigma = 2.2 \times 10^6$). Notice first that agreement between theory and measurement is generally good and secondly that the sphere response is not a simple decaying exponential. (A simple exponential will produce a straight line when plotted with a logarithmic ordinate.) Note also that the receiver amplifier saturates early in time when the input signal

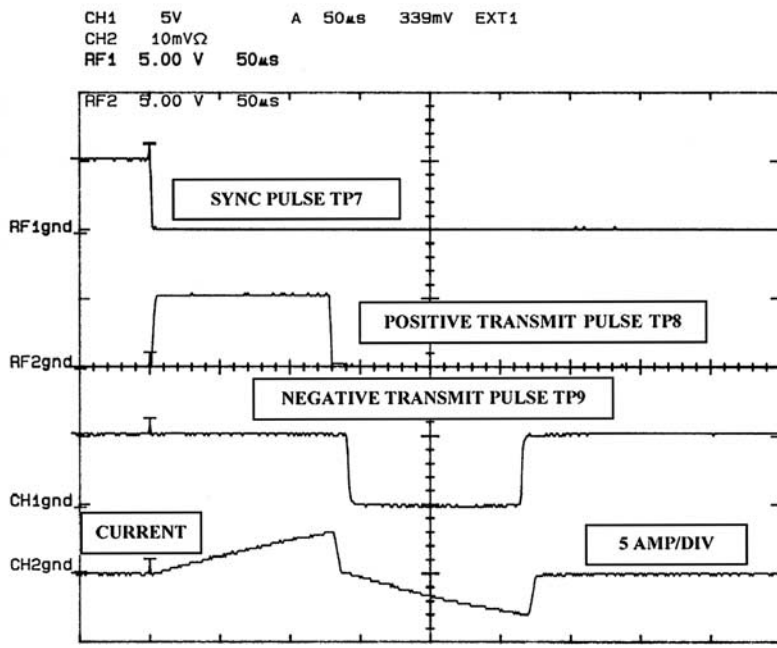

Figure 7. Synchronization pulse TP7, positive TP8 and negative TP9 transmitter voltage pulses, and transmitter coil current waveform.

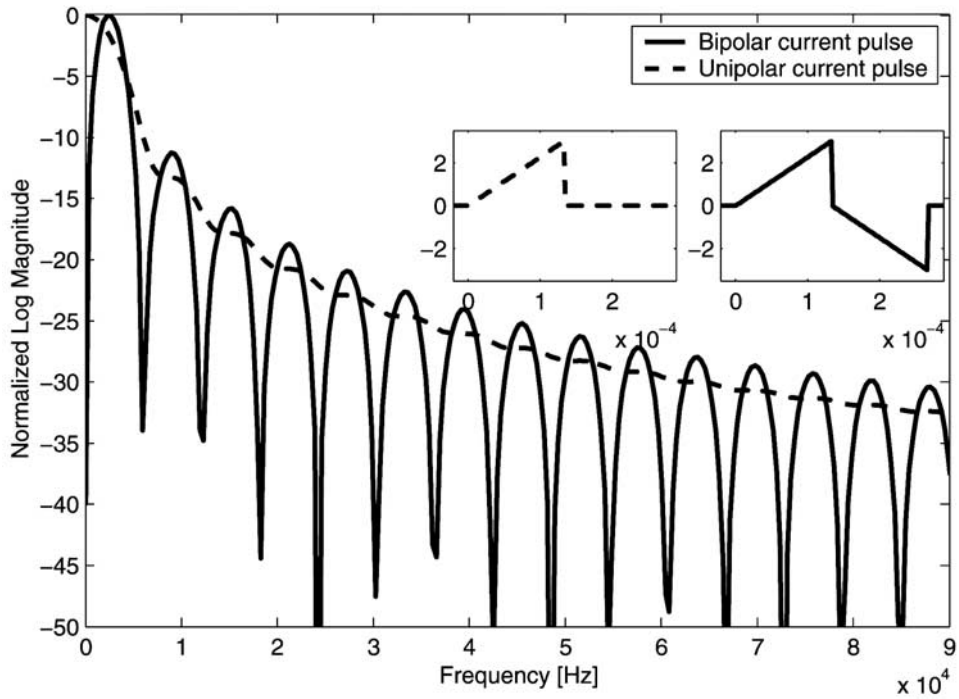

Figure 8. Comparison of bipolar pulse (solid) with unipolar pulse (dashed) in the frequency domain. The bipolar/unipolar waveform is shown in the left/right inset.

strength exceeds the power supply maximum divided by the system gain.

4. Data Collection and Parameter Extraction in Support of Discrimination Experiments

[24] This section describes the data collection efforts with the modified AN/PSS-12 that were conducted at the JUXOCO test site at range 71A, Fort A.P. Hill, Virginia, during the summer months of 2001. As shown in Figure 10, the test site is comprised of a large 20 × 49-m test grid and a smaller 5 × 25 m calibration grid. Both test grids are subdivided into 1 × 1 m grid squares that represent decision opportunities for a detector under test. A land mine or possibly a piece of metallic clutter may be buried at the center of each grid square, while some grid squares are intentionally left empty (blanks). The contents of each square in the calibration lane, known as ground truth, are publicly known, and data collected there are used by researchers to develop discrimination algorithms. The exact contents of the blind grid are known only to U.S. government officials, and they evaluate blind grid declarations and report performance in terms of a probability-of-detection (P_D) versus probability-of-false-alarm (P_{FA}) curve, know in the parlance of probability theory as a receiver operating characteristic (ROC) curve [*Vantrees*, 1968].

[25] A collection of 100 land mines from 13 different mine types were collected to use in the blind grid. The mines are predominantly ''low-metal'' antipersonnel land mines with metallic content by weight ranging from the subgram level up to 18 g. A few large metal-cased antitank land mines with metal content in excess of 2 kg were also used for completeness. Mines buried in the large test grid were identical to those in the calibration lane. Antitank mines are buried up to six inches below the air-soil interface, while antipersonnel mines are typically buried no deeper than three inches. Clutter was acquired during site preparation and represents metallic debris left over from decades of military training and human activity. Examples of the clutter items replanted in the otherwise debris-free test area include rusted shrapnel, expended 50 and 20 mm rounds, rusted nails, pieces of wire, and other unidentifiable metallic pieces.

[26] Figure 11 shows the five measurement positions of the AN/PSS12 search coils relative to an object buried at the center of a 1 × 1 m grid square. The object is at the center of the coils for the first measurement and then between the coils in the north, south, east, and west

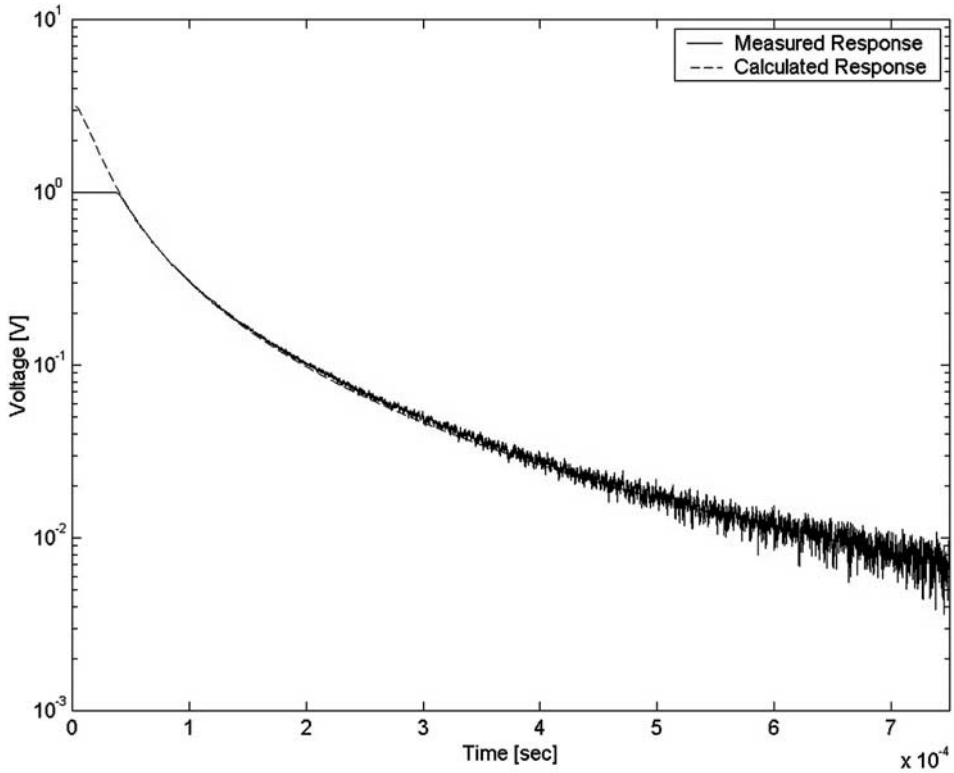

Figure 9. Measured (solid) and calculated (dashed) induction response for a 2-inch diameter chrome-steel sphere.

directions for the remaining four measurements. This strategy ensures that both unique modes (decay rates) of a rotationally symmetric object will be measured [*Baum*, 1999, chap. 7]. In many cases, mines (since they are man-made objects) possess rotational symmetry, and in order to function as intended, they are usually buried with their axis of symmetry, z direction in Figure 11, perpendicular to Earth. Assuming rotational symmetry, at the first measurement location the excitatory magnetic field will lay along the object's symmetry axis (z axis), and likewise the receiver coil will detect only the z-directed object radiated field due to circumferentially directed eddy currents. When the object is between the coils, again assuming rotational symmetry, the north, south, east, and west measurements will be identical, each measuring a linear combination of the object's axial and orthogonal modes. Finally, if the object is not a mine or does not possess rotational symmetry, then the four measurements between the coils will be different. It should be noted that a lack of rotational symmetry does not necessarily imply that the null hypothesis (not mine) is true since some clutter items will certainly be symmetrical (e.g., a spent cartridge oriented vertically), and some mines have asymmetrical oriented metallic parts (Mine Facts; see http://www.humanitarian-demining.org/demining/archive/catalog97/cattrain3.htm).

[27] The measured receiver coil voltage in general has three components: the desired part contributed by the buried metallic object, the component due to direct coupling between the transmitter and receiver coils, and a component due to eddy currents excited in the conducting soil. During the data collection process, a background measurement was made at an outside corner of each grid square. Subtracting a background measurement from a measurement made near an object should result in the desired object-only response, provided the soil in the vicinity of the background measurement is identical to that near the object. Figure 12 shows the total response taken near an M14 mine, background response (blank), and their difference. As expected, the difference response appears as a simple exponentially decaying voltage.

[28] We used the differential correction method described in section 3 to fit an exponential model to the data [*Chapman and Kirk*, 1970]. The returned parameters, exponential decay rates, and amplitudes are the maximum likelihood parameter estimates since the noise has been shown to be white Gaussian [*Riggs et al.*,

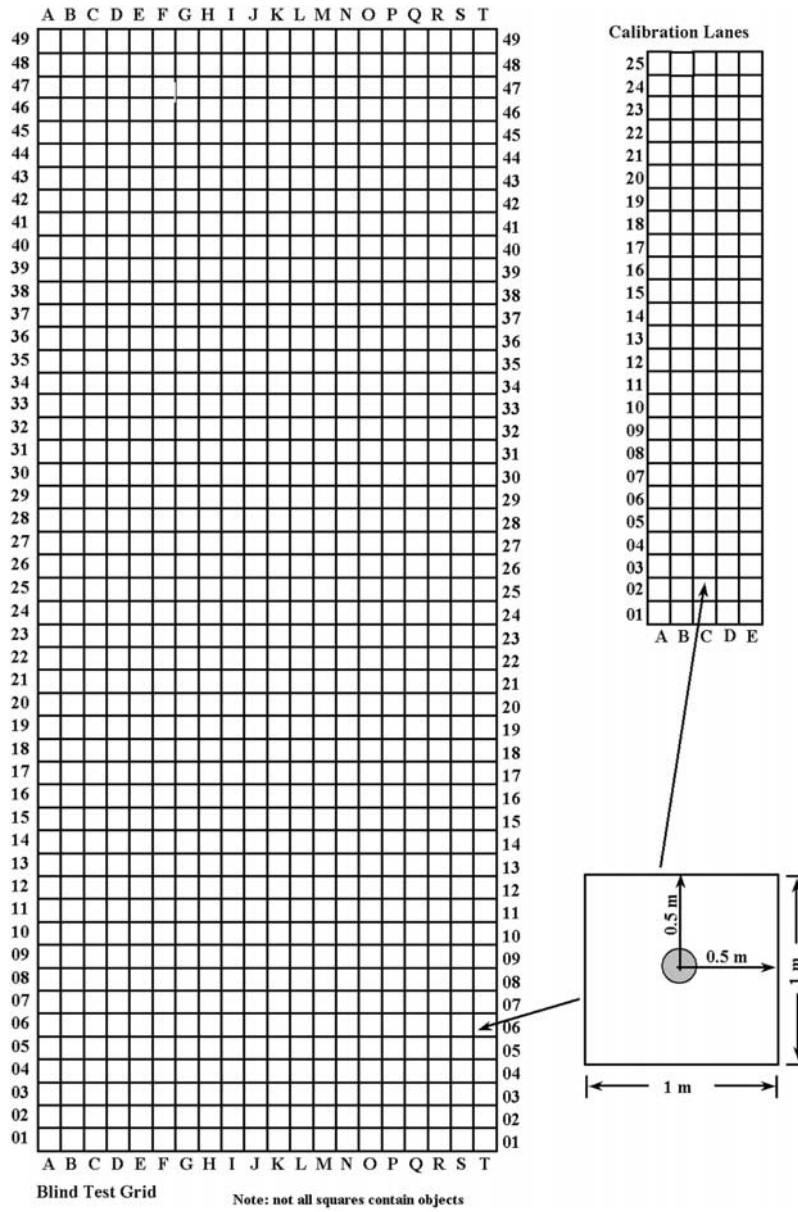

Figure 10. Layout of the calibration and blind test lanes at the hand-held test site at range 71A Fort AP Hill, Virginia.

2001]. Experimentally, it was found that data from small objects could be approximated with good accuracy with a single exponential ($Ae^{-\alpha t}$), while larger objects typically require a sum of two exponentials ($Ae^{-\alpha t} + Be^{-\beta t}$) to achieve a good fit. However, we have shown elsewhere that a single exponential per object produces the best results when discriminating among different conducting objects within a Bayesian hypothesis testing framework [*Riggs et al.*, 2001]. Therefore, on the basis of this experience, all data was fit with a single exponential model. Signal energy, E, was also computed for each waveform using $E = \sum_{i=1}^{N} v_i^2 \Delta t$ with v_i the receiver coil voltage at the ith sample time, the Δt sample period, and the N total number of voltage samples.

[29] Summarizing, five voltage waveforms are measured for each target (center, north, south, east, and west measurement positions) and an energy and decay rate

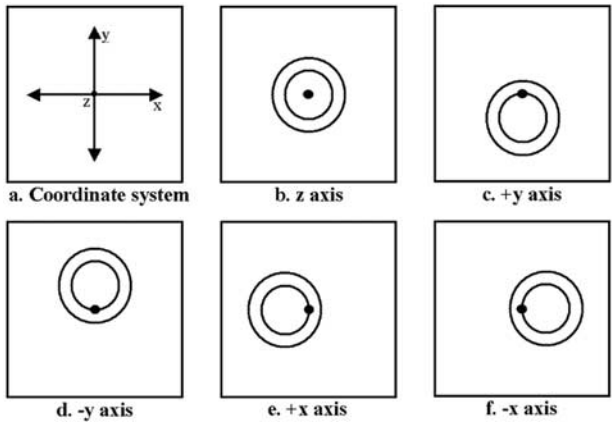

Figure 11. Position of search head relative to the location of the buried object in order to excite and measure a response along all three cardinal axes.

extracted from each measurement, resulting in a total of ten values per mine. A further reduction in data complexity was achieved by averaging the north, south, east, and west measurements, resulting in a single "radial" decay rate and energy. A symmetry parameter was also computed by taking the ratio of decay rates extracted from averaged orthogonal measurements. We refer to this ratio as a symmetry parameter with a value of unity indicating that the object possesses perfect rotational symmetry. All data reduction techniques combined resulted in a total of five parameters per object designated by (sym, d_z, e_z, d_r, e_r) and defined as the symmetry parameter, a decay rate and energy extracted from the center measurement, and a decay rate and energy extracted from the radial averaged measurements. Note that decay rate and energy parameters are considered in log scale.

[30] Figure 13 shows z axis energy and decay rates in log space, extracted from all objects in the blind grid superimposed on the same extracted from selected mines measured in the calibration grid. Observe that there is a discernable group of objects in the blind grid that have z axis decay rates and energies similar to those of the VS-50 mine. Notice also the large cluster of objects at the minimum energy level that span a broad range of decay rates. Low metallic content mines at the maximum burial depth (approximately 3 inches) will exhibit low energy levels and therefore will be difficult to discriminate from small clutter items. A similar plot can be presented for the radial decay rate and energy.

5. Land Mine Discrimination Algorithm Development and Performance

[31] Given the five independent extracted parameters, a decision has to be made regarding the source of those parameters. This is a typical binary hypothesis-testing problem with hypotheses

$$\begin{aligned} \text{clutter}\ \ H_0 &: \sim p(\overline{z}|\Theta_0) \\ \text{mine}\ \ H_1 &: \sim p(\overline{z}|\Theta_1) \end{aligned}, \tag{14}$$

where $\overline{Z}$ is a vector of five independent random variables (sym, d_r, d_z, e_r, e_z) and $\overline{z} = (z_1, z_2, z_3, z_4, z_5)$ is a vector

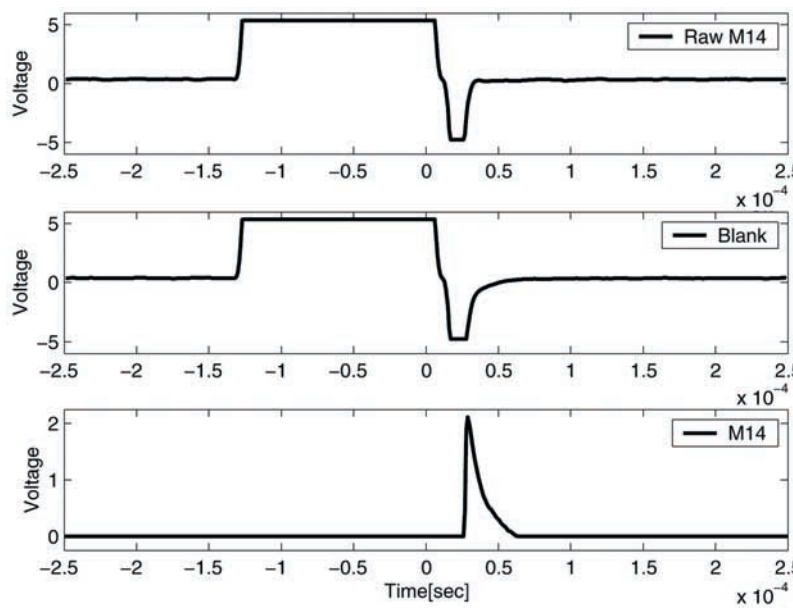

Figure 12. Background subtraction applied to the raw signature of an M14.

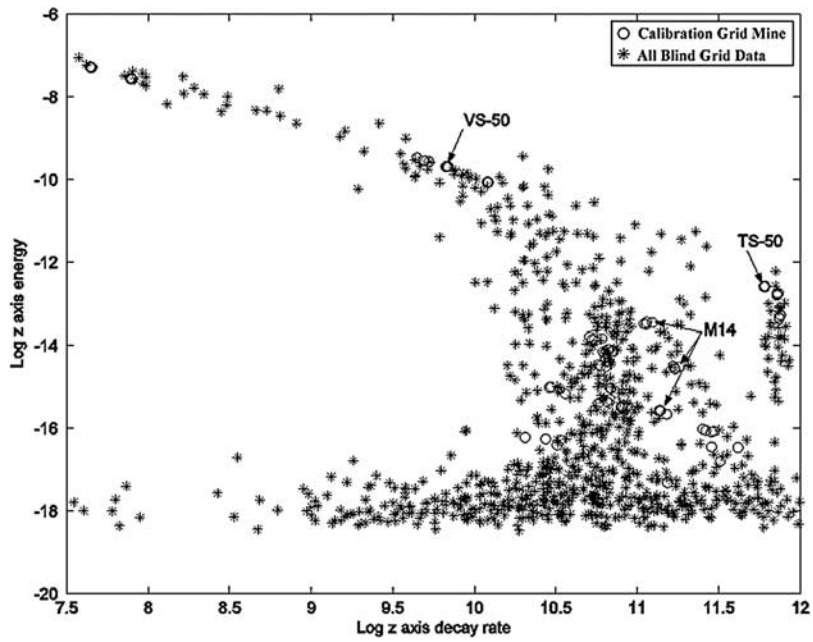

Figure 13. Axial mode decay rate and energy pairs for the calibration grid mines (circles) and all the blind grid items (asterisks). The clusters for three antipersonnel mines are shown.

of observed values of $\overline{Z}$. If p ($\overline{z}$ $|H_i$) is of a known form and is characterized by a set of parameters, $\overline{\theta}$, then $\overline{\Theta}_0$ and $\overline{\Theta}_1$ are the set of values that $\overline{\theta}$ takes under hypotheses H_0 and H_1, respectively. The decision problem thus essentially lies in dividing this five-dimensional observation space into two appropriate regions depending on the Bayes criterion, which results in a likelihood ratio

$$\Lambda(z) = \frac{p(\overline{z}|H_1)}{p(\overline{z}|H_0)} \underset{H_0}{\overset{H_1}{\gtrless}} \eta, \tag{15}$$

where the threshold $\eta = \frac{P(H_0)(C_{10}-C_{00})}{P(H_1)(C_{01}-C_{11})}$. C_{ij} is the cost assigned to the decision H_i when the true hypothesis is H_j. As the ratio of number of mines to clutter in a battlefield is unknown, the prior probabilities, $P(H_0)$ and $P(H_1)$, are unknown. Therefore the threshold is left as a variable quantity.

5.1. Clutter Probability Density Function

[32] As clutter can be of any shape, size, or weight, a uniform distribution of the parameters is assumed. The upper and lower limits of the observation space constitute the limits for the decay rate and energy parameters. From the log space plot (Figure 13), limits of 7.5 and 12 were chosen for decay rates and -18 and -6 for the energies. Correspondingly, the pdfs for the decay rate parameters are given by

$$\begin{aligned} p(z_2|H_0) = p(z_3|H_0) &= \frac{1}{4.5} \\ p(z_4|H_0) = p(z_5|H_0) &= \frac{1}{12}\,. \end{aligned} \tag{16}$$

Since the decay rates can vary over two orders of magnitude, the pdf for the symmetry is defined as

$$p(z_1|H_0) = \frac{1}{100}\,. \tag{17}$$

The pdf that describes the clutter hypothesis is the product of the pdfs of the individual parameters and is given by

$$p(\overline{z}|H_0) = \prod_{i=1}^{5} p(z_i|H_0) = \frac{1}{291,600}\,. \tag{18}$$

5.2. Mine Probability Density Function

[33] The mine data collected from the calibration grid are used as a reference to calculate the pdfs of the parameters under the mine hypothesis. Each parameter is assumed to be Gaussian distributed. Overlapping Gaussian distributions populate each mine cluster. The number of these Gaussians and their mean values are

Table 1. Mean Value Locations for VS-50 Cluster Areas

Point Number	Z Axis Plane, θ_x, θ_y	Orthogonal Axis Plane, ϕ_x, ϕ_y
1	9.69, −9.54	9.32, −9.05
2	9.81, −9.69	9.35, −9.2
3	9.78, −9.64	9.43, −9.30
4	9.88, −9.8	9.53, −9.45
5	9.94, −9.88	9.615, −9.5
6	9.98, −9.95	9.625, −9.58
7	10.07, −10.07	9.73, −9.73
8		9.76, −9.79
9		9.81, −9.85

chosen to ensure that the entire range of mine clusters is covered. The number of Gaussians and their means will, in general, vary with mine type and parameter plane; however, only two unique variance values are used, one for decay rate and another for energy. The variance of the decay rates is chosen to be $\sigma_2^2 = \sigma_3^2 = \sigma_{dr}^2 = 0.05$, and the variance of the energy is chosen to be $\sigma_4^2 = \sigma_5^2 = \sigma_e^2 = 0.1$. The pdfs of the parameters are given by

$$p(z_i|H_1, m_i) = \frac{1}{\sqrt{2\pi\sigma_i^2}} \exp\left[\frac{-(z_i - m_i)^2}{2\sigma_i^2}\right], \qquad (19)$$

where $I = 2, 3, 4, 5$. For example, the VS-50 mine cluster is completely covered by seven standard Gaussians in the axial parameter plane and nine standard Gaussians in the radial parameter plane. The mean value locations form coordinate pairs represented as (θ_x, θ_y) and (ϕ_x, ϕ_y) on the axial and radial parameter planes, respectively. Given these coordinate pairs, the pdfs of the parameters are

$$\begin{aligned}
p(z_2|H_1, \theta_x) &= \frac{1}{\sqrt{2\pi\sigma_{dr}^2}} \exp\left[\frac{-(z_2 - \theta_x)^2}{2\sigma_{dr}^2}\right] \\
p(z_3|H_1, \phi_x) &= \frac{1}{\sqrt{2\pi\sigma_{dr}^2}} \exp\left[\frac{-(z_3 - \phi_x)^2}{2\sigma_{dr}^2}\right] \\
p(z_4|H_1, \theta_y) &= \frac{1}{\sqrt{2\pi\sigma_e^2}} \exp\left[\frac{-(z_4 - \theta_y)^2}{2\sigma_e^2}\right] \\
p(z_5|H_1, \phi_y) &= \frac{1}{\sqrt{2\pi\sigma_e^2}} \exp\left[\frac{-(z_5 - \phi_y)^2}{2\sigma_e^2}\right].
\end{aligned} \qquad (20)$$

The coordinate pairs for the VS-50 are shown in Table 1.

[34] The pdf for the symmetry parameter is assumed to be a Gaussian density function with mean one and variance, $\sigma_{sym}^2 = 0.1$.

$$p(z_1|H_1) = \frac{1}{\sqrt{2\pi\sigma_{sym}^2}} \exp\left[\frac{-(z_1 - 1.0)^2}{2\sigma_{sym}^2}\right] \qquad (21)$$

The product of the individual parameter density functions describes the mine hypothesis probability density function and is given by

$$\begin{aligned}
p(\bar{z}|H_1, \bar{\theta}, \bar{\phi}) &= \frac{1}{\sqrt{(2\pi)^5 \sigma_{dr}^2 \sigma_e^2 \sigma_{sym}}} \\
&\cdot \exp\left[\begin{array}{l} \dfrac{-(z_1 - 1.0)^2}{2\sigma_{sym}^2} - \dfrac{(z_2 - \theta_x)^2}{2\sigma_{dr}^2} - \dfrac{(z_3 - \phi_x)^2}{2\sigma_{dr}^2} \\ - \dfrac{(z_4 - \theta_y)^2}{2\sigma_e^2} - \dfrac{(z_5 - \phi_y)^2}{2\sigma_e^2} \end{array}\right],
\end{aligned} \qquad (22)$$

where $\bar{\theta}$ corresponds to (θ_x, θ_y) and $\bar{\phi}$ corresponds to (ϕ_x, ϕ_y).

5.3. Likelihood Ratio Test

[35] Now that we have the pdfs describing each hypothesis, Bayes criterion (15) may be written as

$$\begin{aligned}
\Lambda(z) &= \frac{p(\bar{z}|H_1)}{p(\bar{z}|H_0)} \\
&= \frac{\int_{\bar{\phi}} \int_{\bar{\theta}} p(\bar{z}|\bar{\theta}, \bar{\phi}) p(\bar{\theta}|H_1) p(\bar{\phi}|H_1) d\bar{\theta} d\bar{\phi}}{p(\bar{z}|H_0)} \begin{array}{l} H_1 \\ \geq \\ < \\ H_0 \end{array} \eta.
\end{aligned} \qquad (23)$$

If $\bar{\theta}$ and $\bar{\phi}$ are assumed to be random variables with unknown distributions, $p(\bar{\theta}|H_1)$ and $p(\bar{\phi}|H_1)$ are unknown, and therefore $p(\bar{z}|H_1)$ is also unknown. The test procedure to be used for this kind of problem is not specified. Therefore, $=\bar{\theta}$ and $\bar{\phi}$ must be assigned a particular range of values for each mine cluster, and the LRT is tested for a uniformly most powerful (UMP) test. For this case the LRT depends on knowledge of $\bar{\theta}$ and $\bar{\phi}$, so a UMP does not exist [*Srinath et al.*, 1996]. The maximum likelihood estimates of $\bar{\theta}$ and $\bar{\phi}$ obtained by maximizing $p(\bar{z}|\bar{\theta}, \bar{\phi})$ are used as the true values in the LRT. The resulting generalized likelihood ratio test (GLRT) is written as

$$\Lambda_g(\bar{z}) = \frac{\max_{\bar{\theta} \in (\theta_x, \theta_y)} \max_{\bar{\phi} \in (\phi_x, \phi_y)} p(\bar{z}|\theta, \phi)}{p(\bar{z}|H_0)} \begin{array}{l} H_1 \\ \geq \\ < \\ H_0 \end{array} \eta, \qquad (24)$$

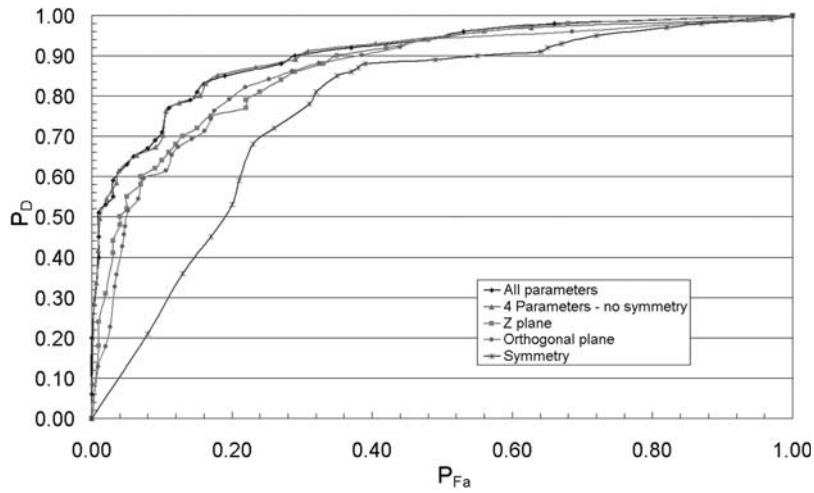

Figure 14. ROC curves for the blind grid. See color version of this figure at back of this issue.

where $p(\bar{z}|H_0) = \frac{1}{291,600}$ is a constant, and the GLRT may be redefined as

$$\Lambda_g(\bar{z}) = \max_{\bar{\theta}\in(\theta_x,\theta_y)} \max_{\bar{\phi}\in(\phi_x,\phi_y)} p(\bar{z}|\theta,\phi) \underset{H_0}{\overset{H_1}{\gtrless}} \eta' = \frac{\eta}{291,600}. \tag{25}$$

The density function $p(\bar{z}|\theta, \phi)$ is computed for every mean value coordinate pair $\bar{\theta}$ and $\bar{\phi}$, and the maximum value of all the computed probabilities for a single observation is retained as the GLRT test result. The result is then compared to the threshold to determine if the observation came from a mine or a clutter item.

5.4. Results

[36] The ROC curve results for the GLRT applied to the blind grid data are shown in Figure 14. Five plots are presented to show the performance of the algorithm using different subsets of the available five parameters. The ROC curve of the GLRT using only the symmetry parameter is well above the chance diagonal but has the lowest overall performance. The ROC curves for the GLRT using the axial parameters alone and using radial parameters alone are almost identical and have a better performance than the symmetry parameter alone. This implies that both axial and radial parameters play an equal role in discrimination. There is a reasonable improvement when both radial and axial parameters are utilized. This indicates that although some clutter items have the same response as a mine for some excitation orientations, they typically will not have the same response for all excitation orientations. The performance does not improve when the symmetry parameter is added to the decay rate/energy parameters. This observation implies that either symmetry is an inferior discrimination feature compared to the decay rate or energy parameters or the remaining four parameters already contain the symmetry information. The best performance of the ROC curves show that the GLRT achieves a P_D of 50% with a P_{FA} of near 0%. After this point the performance degrades and the GLRT gradually achieves a P_D of 90% with a P_{FA} of 30% and then even more gradually achieves a P_D of 100% with a P_{FA} of 100%. The reason for this might be that the coupling strength of most of the mines is low either because of a very low metallic content or because they are buried deep or both.

6. Summary

[37] This paper has demonstrated that only minor modifications to the AN/PSS-12 were necessary in order construct an EMI device with at least some ability to discriminate between mines and clutter. Other sensor designs might offer better performance, especially if they can provide improved signal-to-noise ratio for deeply buried low metallic content mines. Reasonable performance depends on one's ability to measure all unique components of an object's polarizability tensor. This in turn requires that the search head be positioned carefully with respect to the target's center of mass. At the JUXOCO test site, all targets are buried at the center of each grid obviating the need to locate the target center. Certain search coil designs are better for locating a target center than others. For example, a search head consisting of a circular

Figure A1. U.S. Army's hand-held metal detector, AN/PSS-12.

transmitter coil circumscribing a figure eight receiver coil is described in the work of *Kingdon et al.* [2004]. The receiver coil is wrapped in a bucking configuration so the received signal polarity changes rapidly as the target pass along a line of symmetry between the coils. Thus the center of the search coil can be easily aligned with the target center. The bucking configuration has the added advantage of substantially reducing direct coupling between transmitter and receiver coils, essentially allowing one to measure the target only response closer in time to when the transmitter current is turned off. This ultimately leads to improved signal-to-noise ratio [*Nelson et al.*, 2001]. It is important to mention that others (in particular, researchers at Duke University [*Collins et al.*, 1999], Johns Hopkins [*Nelson and Huynh*, 2001], and AETC Inc. [*Bell et al.*, 1998]) have also conducted successful discrimination experiments. Although discrimination has been successfully demonstrated, the state of the art is still somewhat immature. In particular, ''real-time'' discrimination based on EMI response only has yet to be demonstrated, and questions remain as to the best way to present the operator with the additional information available from advanced sensors and signal processing algorithms. These challenges will no doubt some day be addressed.

Appendix A

A1. Overview of the Fundamental Operating Characteristics of the AN/PSS-12

[38] The purpose of this appendix is to describe the operation of the AN/PSS-12 as a pulse induction metal detector. In the body of the report we describe modifications to the AN/PSS-12 circuitry that were necessary to carry out the discrimination experiments that are the focus of this paper.

[39] As previously mentioned, Schiebel Corporation of Austria manufactures the U.S. Army's currently fielded metal detector. Schiebel refers to the detector as the AN-19/2, while the U.S. Army uses the designation AN/PSS-12. As shown in Figure A1, the AN/PSS-12 search head uses two concentric coils; the outer is used to transmit (25.5 cm diameter) and the inner (18.5 cm diameter) to receive. As described above, the AN/PSS-12 is a pulse induction metal detector.

A2. Transmitter Description

[40] This section provides an explanation of the electric current excitation waveform used in the AN/PSS-12. Referring to the block diagram in Figure A2 and the corresponding waveforms of Figure 7, the synchronization pulse available on test pin 7 (TP7) initiates one complete transmit-receive cycle lasting approximately 15 ms (67 Hz repetition rate). According to waveforms shown in Figure 7, the fall of voltage on TP7 initiates a positive voltage pulse on TP8 and a subsequent negative voltage pulse on TP9. As can be seen from Figure 7, the duration of the positive pulse (TP8) is approximately 120 μs and begins with the falling edge of the synchronization pulse. The duration of the negative pulse (TP9) is the same as that of the positive pulse, 120 μs; however, it is initiated 130 μs after the fall of the synchronization pulse. The positive and negative voltage pulses (TP8 and TP9) are driven into the transmitter coil resulting in the triangular shaped current waveform shown in Figure 7. In accordance with Faraday's law of induction, the transmitter current linearly increases from zero to a maximum value of approximately 3 amps and then drops abruptly to zero. Following the positive current ramp, the current linearly decreases from zero to approximately minus 3 amps and then once again drops abruptly to zero. The measurements shown in Figure 7 were made

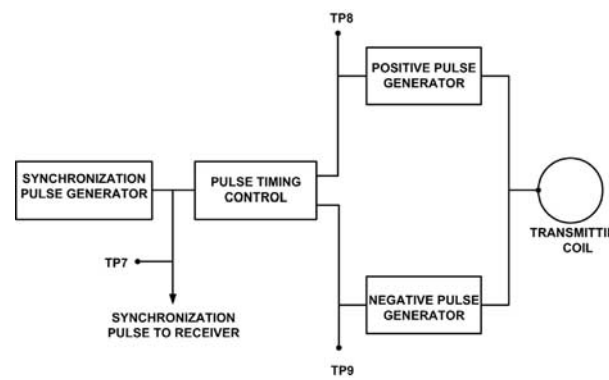

Figure A2. Transmitter block diagram for the AN/PSS-12.

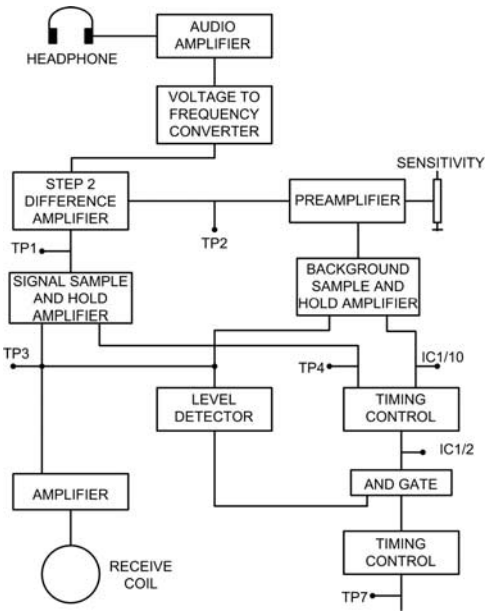

Figure A3. Receiver block diagram for AN/PSS-12.

with a Tektronix 2430A digital oscilloscope and a TM502A current probe.

A3. Receiver Description

[41] Currents that flow in the transmitter coil and eddy currents that flow in the object each induce a voltage into the receiver coil. The receiver circuitry of the AN/PSS-12 amplifies and processes this voltage to provide the operator with a warning tone whenever a metallic object is near the search head. A simplified block diagram of the AN/PSS-12's receiver circuitry is shown in Figure A3. The block diagram indicates that the voltage at test pin 3 (TP3) is at the output of the first stage of amplification after the receiving coil. Figure A4 shows the voltage at TP3 with and without a metallic object placed near the search head. Between the vertical dashed markers the TP3 voltage waveforms are identical. The TP3 waveforms during this 293 μs period have a square wave shape because the voltage induced into the receiver coil is (by consequence of Faraday's law of induction), proportional to the time rate of change of the current driven into the transmitting coil. After the 293 μs period the object and no-object waveforms are different. In particular, following the second dashed marker the no-object response quickly decays to a steady state value of 2.35 volts. However, with the object present the first stage amplifier remains saturated at near zero volts for a duration of approximately 200 μs following the second dashed marker. After this saturation period the response once again decays to the steady state value of 2.35 volts. As described in greater detail below, the receiver circuitry compares a sample of the decaying portion of the TP3 voltage to a threshold in order to indicate if a metallic object is present.

[42] Figure A5 presents the voltage waveforms measured at test pins 7 (TP7), 3 (TP3), and 4 (TP4) and on

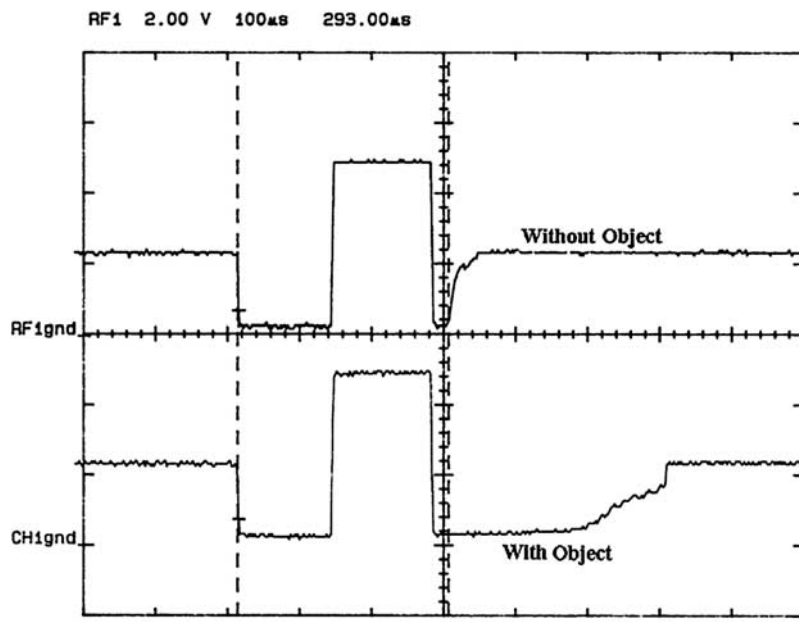

Figure A4. Amplified receiver coil voltage TP3 with and without a metallic object placed near the search head.

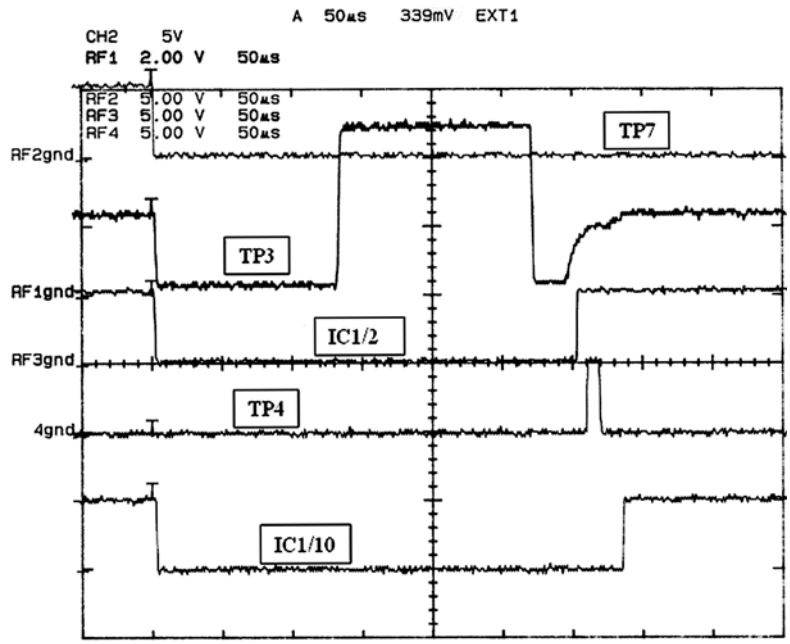

Figure A5. Synchronization pulse TP7, amplified receiver coil voltage TP3, timing waveform IC1/2, timing waveform TP4, and timing waveform IC1/10.

pins 2 and 10 of integrated circuit 1 (IC1/2 and IC1/10). The top most curve of Figure A5 is the synchronization pulse (TP7) that is also used in the transmitter circuitry (see discussion above). The first waveform below the synchronization pulse is the amplified receiver coil voltage on TP3 just described. Recall that the detection process depends on voltage samples taken during the decaying portion of the TP3 curve.

[43] With reference to Figure A3, the receiver employs two sample-and-hold amplifiers. The signal sample-and-hold amplifier only samples during the decaying portion of the TP3 waveform. The background sample-and-hold amplifier only samples after the transmitter current pulse is extinguished and the TP3 voltage has returned to its steady state value.

[44] According to Figure A5, the voltage waveform on IC1/2 falls to zero with the synchronization pulse and stays low until the decaying portion of the TP3 waveform reaches 1.5 volts, at which time, through the use of a level detector, it transitions high again. When the IC1/2 voltage transitions high it initiates, after a 10 μs delay, a voltage pulse on TP4 of 10 μs duration. The unity-gain sample-and-hold amplifier in Figure A3 samples during this 10 μs window. Summarizing, timing pulses available on IC1/2 and TP4 are utilized so that the signal sample-and-hold amplifier samples when the TP4 voltage is "high" which always occurs during the decaying portion of the TP3 voltage.

[45] The waveform on pin 10 of integrated circuit 1 (IC1/10) also falls low with the synchronization pulse (TP7) and transitions high again only after the TP3 voltage has decayed to its steady state value of 2.35 volts. The timing waveform IC1/10 is designed to transition high 15 μs after the falling edge of the pulse on TP4 thus insuring that the IC1/10 waveform is high only when transmitter currents and eddy currents on the object are zero. The background sample-and-hold amplifier samples when the IC1/10 voltage is high so that only the no-object receiver coil signal is sampled.

[46] In the block diagram of Figure A3, the background sample-and-hold amplifier is AC coupled to the receiver coil amplifier so that background signal fluctuations around zero volts are sampled. The gain of the preamplifier following the background sample-and-hold amplifier is controlled by the position of the sensitivity knob. In order to tune the detector for maximum sensitivity, the preamplifier gain must be adjusted manually so that its output voltage is equal to the output voltage of the signal sample-and-hold amplifier. This adjustment is made with no metallic objects near the search head. In short, with no object present, the sensitivity knob should be adjusted so that the voltage at TP1 and TP2 are approximately equal.

[47] The output of the step 2 difference amplifier increases nonlinearly as the difference between its two inputs increases. From Figure A3, the two inputs to the

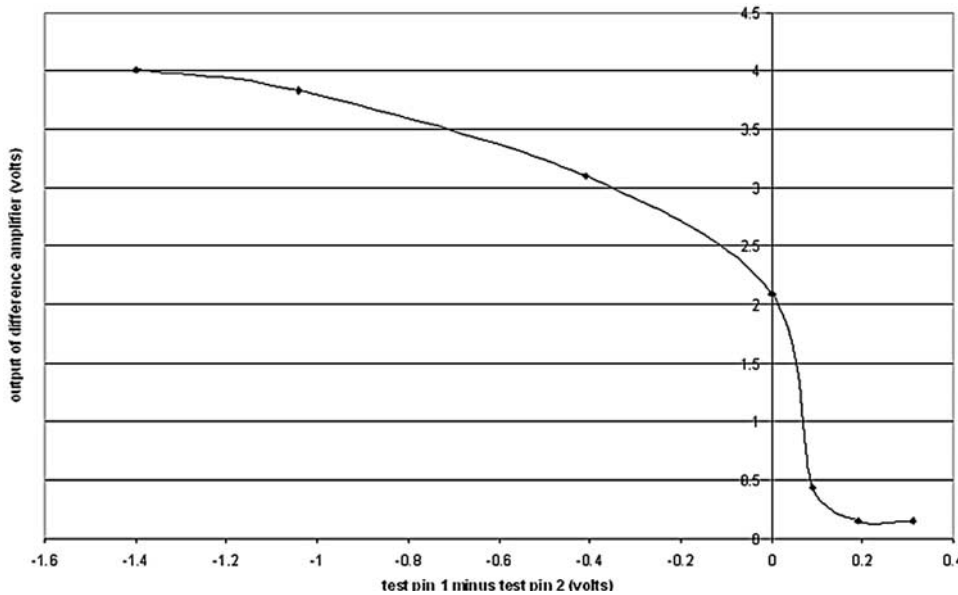

Figure A6. Voltage transfer function for the step 2 difference amplifier.

step 2 amplifier are seen to be the outputs from the signal and level-shifted background sample-and-hold amplifiers. Note that once the sensitivity knob has been properly adjusted the voltage on TP2, one of the inputs to the difference amplifier, remains approximately constant. When, owing to a nearby metallic object, the TP1 signal input to the difference amplifier changes, the output of the step 2 difference amplifier will increase thereby driving the voltage-to-frequency converter to produce an audio tone with a frequency above the background "click" rate.

[48] Figure A6 illustrates the nonlinear transfer characteristics of the step 2 difference amplifier. One can see that the output of the difference amplifier increases very rapidly when its input is smaller than a threshold around 0.1 volts. As the input decreases further below the 0.1 volt threshold, the output voltage increases less rapidly. Figure A7 illustrates the transfer characteristics

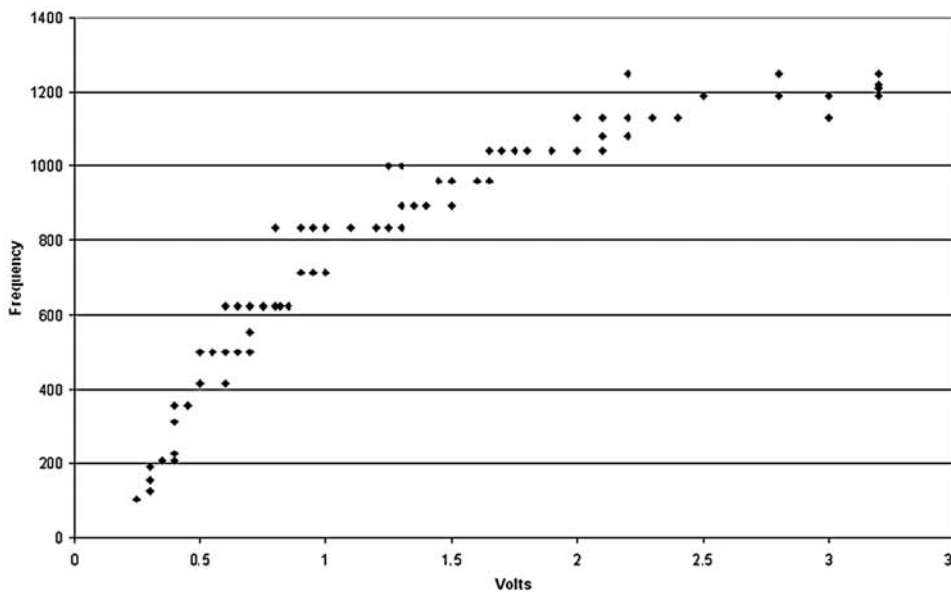

Figure A7. Transfer characteristics for the voltage-to-frequency converter.

of the voltage-to-frequency converter. As the input to the voltage-to-frequency converter ranges from 0.25 to 3.5 volts, its output frequency increases from 100 to 1200 Hz. The transfer functions of Figures A6 and A7 indicate that small changes relative to the fixed background signal will create a rapid increase in audio output frequency. In fact, only a slight increase over the 0.1-volt threshold of Figure A6 causes the audio output tone to "jump" from 100 to 1000 Hz!

References

Baum, C. E. (1999), *Detection and Identification of Visually Obscured Targets*, Taylor and Francis, Philadelphia, Pa.

Bell, T. H., B. Barrow, and N. Khadr (1998), Shape-based classification and discrimination of subsurface objects using electromagnetic induction, paper presented at International Geoscience and Remote Sensing Symposium (IGARS '98), Geosci. and Remote Sens. Soc., Seattle, Wash.

Candy, B. H. (1996), Pulse induction time domain metal detector, Patent 5576624, U.S. Patent and Trademark Off., Washington, D. C.

Carin, L., H. Yu, Y. Dalichaouch, A. R. Perry, P. V. Czipott, and C. E. Baum (2001), On the wideband EMI response of a rotationally symmetric permeable and conducting target, *IEEE Trans. Geosci. Remote Sensing*, *39*(6), 1206–1213.

Chapman, G. T., and D. B. Kirk (1970), A method for extracting aerodynamic coefficients from free-flight data, *AIAA J.*, *8*, 753–758.

Collins, L., P. Gao, and L. Carin (1999), An improved Bayesian decision theoretic approach for land mine detection, *IEEE Trans. Geosci. Remote Sens.*, *37*(2), 811–819.

Corbyn, J. A. (1980), Pulse induction metal detector, *Wireless World*, *86*, 40–44.

Das, Y., J. D. Toews, K. Russell, and S. Lewis (2000), Results of in-air testing of metal detectors, *Tech. Rep.*, Def. Res. Estab., Suffield, Ottawa, Ont.

Grant, F. S., and G. F. West (1965), *Interpretation Theory in Applied Geophysics*, McGraw-Hill, New York.

Kingdon, J., N. Khadr, T. Bell, and L. Riggs (2004), Development of an electromagnetic induction sensor for land mine discrimination, paper presented at SAGEEP 2004 Conference, Environ. and Eng. Geophys. Soc., Colorado Springs, Colo., 22–26 Feb.

Liao, X., and L. Carin (2004), Application of the theory of optimal experiments to adaptive electromagnetic-induction sensing of buried targets, *IEEE Trans. Pattern Anal. Mach. Intell.*, in press.

Lowe, L. T. (2001), Enhanced land mine discrimination using the multi-axis electromagnetic induction response of a buried finitely conducting object, Ph.D. thesis, Auburn Univ., Auburn, Ala.

MacDonald, J., et al. (2003), *Alternatives for Land mine Detection*, RAND, Santa Monica, Calif.

Nelson, C. V., and T. B. Huynh (2001), Wide bandwidth, time decay responses from low-metal mines and ground voids, in *Detection and Remediation Technologies for Mines and Minelike Targets*, vol. VI, edited by A. C. Dubey et al., pp. 55–64, Int. Soc. for Opt. Eng., Bellingham, Wash.

Nelson, C. V., C. B. Cooperman, W. Schneider, D. S. Wenstrand, and D. G. Smith (2001), Wide bandwidth time-domain electromagnetic sensor for metal target classification, *IEEE Trans. Geosci. Remote Sensing*, *39*(6), 1129–1138.

Riggs, L. S. (1999), Red team final report: Comparison of the sensitivity of five commonly used metal detectors, *Final Rep.*, U.S. Army CECOM RDEC, Night Vision and Electron. Sensors Dir., Fort Belvoir, Va.

Riggs, L. S., J. E. Mooney, and D. E. Lawrence (2001), Identification of metallic mine-like objects using low frequency magnetic fields, *IEEE Trans. Geosci. Remote Sensing*, *39*(1), 56–66.

Srinath, M. D., P. K. Rajasekaran, and R. Viswanathan (1996), *Introduction to Statistical Signal Processing with*, Prentice-Hall, Old Tappan, N. J.

Vantrees, H. (1968), *Detection, Estimation, and Modulation Theory*, John Wiley, Hoboken, N. J.

Won, I. J., D. A. Keiswetter, D. R. Hansen, E. Novikova, and T. Hall (1997), GEM-3: A monostatic broadband electromagnetic induction sensor, *J. Environ. Eng. Geophys.*, *2*, 53–64.

S. Chilaka and L. Riggs, Electrical and Computer Engineering Department, Auburn University, Auburn, AL 36849, USA. (riggs@eng.auburn.edu)

L. Collins, Electrical and Computer Engineering Department, Duke University, Durham, NC 27708, USA.

L. Lowe, Phase IV Systems, 3405 Triana Boulevard, Huntsville, AL 35805, USA.

R. Weaver, Night Vision and Electronic Sensors Directorate, 10221 Burbeck Rd., Fort Belvoir, VA 22060, USA.

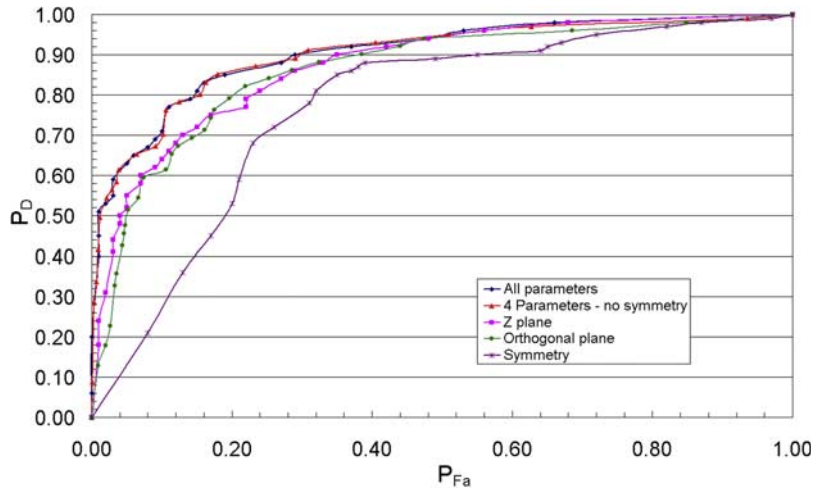

Figure 14. ROC curves for the blind grid.